nature communications

Article

https://doi.org/10.1038/s41467-026-68921-3

Clonal expansion of cytotoxic CD8+ T cells in lecanemab-associated ARIA

Received: 25 November 2025

Accepted: 21 January 2026

Published online: 30 January 2026

Check for updates

Lance A. Johnson[1,2], Kai Saito[1], Akhil V. Pallerla[2], Jessica L. Funnell[2], Ashley R. Ezzo[3], Chelsea M. Song[3], Douglas A. Harrison[4], Noah J. Norton[1], Lauren C. Moore[1,5], Linda J. Van Eldik[1,5], David W. Fardo[1,6], Greg E. Cooper[7] & Josh M. Morganti[1,5]

Amyloid-related imaging abnormalities (ARIA) are the principal safety concern limiting anti-amyloid therapies for Alzheimer's disease, yet their biology remains unclear. Here we show, through multi-omic profiling of peripheral blood from three ARIA+ patients and matched controls, that ARIA is associated with coordinated reprogramming of CD8 + T cells. CD8+ effector memory (TEM) and terminally differentiated (TEMRA) subsets were expanded, clonally enriched, and transcriptionally primed for cytotoxicity and vascular trafficking. Transcription factor inference and metabolomics converged on glycolytic reprogramming favoring short-lived effector function. Ligand-receptor modeling revealed enhanced monocyte-to-T cell signaling through antigen presentation, adhesion, and chemokine axes, while integration with a cerebrovascular atlas confirmed that ARIA-associated TEMRAs are transcriptionally "addressed" for vascular engagement. Together, these findings identify a peripheral immune signature linking metabolic reprogramming, clonal CD8+ expansion, and altered intercellular communication to ARIA, with implications for biomarker development and risk mitigation pending validation in larger cohorts.

Alzheimer's disease (AD) is the leading cause of dementia worldwide, accounting for 60–80% of all documented dementia cases. In 2023, the first disease modifying therapeutic was fully approved by the FDA for use in treatment of AD. Lecanemab (Leqembi®), an anti-amyloid beta (Aβ) monoclonal antibody selective for soluble protofibrils, is remarkably efficient in clearing amyloid from the brain, and modestly slows the cognitive decline associated with AD[1]. However, treatment is sometimes accompanied by amyloid-related imaging abnormalities (ARIA), including vasogenic edema/effusions (ARIA-E) and microhemorrhages/siderosis (ARIA-H)[1,2]. With safety a key determining factor for both patients and providers and a high burden of MRI-based monitoring, access to and adoption of anti-amyloid therapies have been slowed by concerns over ARIA risk.

Susceptibility to ARIA is not uniform and its underlying mechanism(s) remain unknown. Current data indicate a strong Apolipoprotein E (*APOE*) ε4 gene-dose effect on ARIA incidence, motivating pre-treatment genotyping and intensified MRI monitoring in ε4 carriers[3–5]. Case reports describe hemorrhages after thrombolysis[6] and fatal β-amyloid–related arteritis[7], both cases in *APOE* ε4/ε4 individuals. Collectively, these observations implicate an immune–vascular mechanism for ARIA and raise the question of whether circulating peripheral blood mononuclear cell (PBMC) signatures can forecast

[1]Sanders-Brown Center on Aging, University of Kentucky College of Medicine, Lexington, KY, USA. [2]Department of Physiology, University of Kentucky College of Medicine, Lexington, KY, USA. [3]Norton Research Institute, Norton Healthcare, Louisville, KY, USA. [4]Department of Biology, University of Kentucky College of Arts & Sciences, Lexington, KY, USA. [5]Department of Neuroscience, University of Kentucky College of Medicine, Lexington, KY, USA. [6]Department of Biostatistics, University of Kentucky College of Public Health, Lexington, KY, USA. [7]Norton Neuroscience Institute, Norton Healthcare, Louisville, KY, USA. e-mail: josh.morganti@uky.edu

ARIA risk and clarify its biology. Because lecanemab is delivered systemically and ARIA risk peaks early, dynamic immune responses in the blood are both biologically relevant to cerebral events and practically measurable at the time when risk is greatest.

In this report, we describe a case-control study of three sex, age, and *APOE* genotype matched pairs of AD patients undergoing treatment with lecanemab at a regional medical center[8]. Using next-generation sequencing techniques, including single-cell (sc) RNA sequencing (seq), CITE-seq, V(D)J, and targeted metabolomics we identify a unique immunometabolic profile of subjects who develop ARIA, compared to those who do not. Specifically, PBMCs from ARIA+ patients feature expanded $CD8^+$ T cell subsets and increased clonal expansion of $CD8^+$ T-Effector Memory expressing CD45RA (TEMRA) cells. These ARIA+ PBMCs are transcriptionally distinct, enriched for pro-glycolytic genes and metabolites, and spatially map to brains of AD patients treated with active and passive Aβ immunization[9]. Together, these clinical data highlight a T-cell mediated mechanism that may inform future studies and aid in the development of safer and more effective therapeutics for the highest risk AD populations.

Results

Expansion of cytotoxic CD8 subsets defines the ARIA immune signature

Six individuals receiving bi-weekly infusions (10 mg/kg) of lecanemab were recruited from Norton Neuroscience Institute Memory Clinic (Louisville, KY)[8]. We selected three subjects with radiographically confirmed ARIA, including one case of ARIA-E + , one ARIA-H + , and one ARIA E + /H+ case (Fig. 1a). Controls were matched by age (± 2–5 years), sex, *APOE* genotype, and lecanemab infusion number (±1); none of the individuals were taking additional immunotherapies (Supplemental Table 1). To establish the clinical context of our cohort, we first confirmed the presence of amyloid-related imaging abnormalities (ARIA) on serial MRI scans. Representative cases demonstrate ARIA-E, detected on T2-weighted fluid-attenuated inversion recovery (FLAIR/TIRM) imaging, and/or ARIA-H, detected on susceptibility-weighted imaging (SWI) (Fig. 1a).

To capture the peripheral immune repertoire, we performed multi-omic profiling of PBMCs from ARIA case-controls using single-cell RNA sequencing, CITE-seq, V(D)J clonotyping, and metabolomic profiling (Fig. 1b). Unsupervised clustering (integrated on RNA and surface protein expression) revealed the expected diversity of immune lineages across T lymphocytes ($CD3^+CD4^+$ and $CD3^+CD8^+$), B lymphocytes ($CD19^+$), monocytes ($CD14^+$ and $CD16^+$), plasmacytoid ($Fc\epsilon R1\alpha^+$) and conventional ($CD11c^+$) dendritic cells, natural killer cells ($CD56^+$) and platelets (CD62p)(Fig. 1c, d). Examining proportional changes across these cell types revealed an overall increase in the amount of $CD8^+$ T cells in the $ARIA^+$ samples (Fig. 1e; purple) with a concomitant decrease in $CD4^+$ T cells (Fig. 1e; red). Similarly, clinical blood work showed no difference in red or white blood cell counts, although an absolute lymphocyte count suggested an increase in ARIA+ subjects (Fig. 1f).

To examine proportional shifts beyond the generalized CD4 versus CD8 dichotomization, we subsetted and re-clustered $CD4^+$ and $CD8^+$ T cells to reveal 65,481 cells across 16 states in the integrated RNA + surface protein latent space (Fig. 1g). Cell-surface protein expression was used to corroborate RNA signatures and define the 16 states (Fig. 1h). Within the $CD8^+$ compartment, comparative analysis showed a relative expansion of naïve cells (Naive; $CD45RA^+$, $CD62L^+$; $CCR7^+$, $SELL^+$), effector memory (TEM; $CD45RO^+$, $GZMA^+$, $CCL5^+$), with the largest proportional increases observed in terminally differentiated effector memory (TEMRA; $CD45RA^+$, $KLRG1^+$, $GNLY^+$, $GZMB^+$) (Fig. 1i-k).

To evaluate whether these compositional changes were accompanied by transcriptional differences, we performed Fisher's meta-analysis comparing TEMRAs from ARIA+ versus ARIA- samples (Fig. 1l). TEMRA cells from $ARIA^+$ patients displayed a coordinated effector program: upregulated cytotoxic/Fc-receptor signaling (*STX11, FCGR3A, LYN/FGR/PLCG2*) and chemokine/migratory machinery (*CCL3, CYRIA, SLC16A3*) favoring vascular trafficking and sustained activity. The TEMRA cells from ARIA+ patients also expressed MHC-II genes (*HLA-DRB1/-DQA1/-DQB1/-DRB5*) and inhibitory/stress transcripts (*LILRB1, CISH, CDKN1A*), consistent with chronic antigenic stimulation alongside effector programming. These findings echo TEMRA biology in aging/chronic inflammation and multiple sclerosis (MS), where clonally expanded $CD8^+$ TEMRA/Tissue Resident Memory (TRM) cells accumulate at perivascular/meningeal sites and can injure endothelium[10–12]. Together, these results indicate that TEMRAs in ARIA + patients adopt a unique transcriptional profile marked by effector function, migratory capacity, chronic activation, and a shifted metabolic signature.

An additional feature of ARIA+ TEMRAs was enrichment of metabolic regulators (down: *LDHB*; up: *GLUL*, *LDHA*, and the lactate and glutamine exporters *SLC16A3* and *SLC1A5*) indicating a pro-glycolytic, glutamine-fueled metabolism that supports sustained effector activity (Fig. 1l)[13]. To determine whether group-level transcriptional differences reflected consistent changes across all ARIA+ cases or were driven by individual outliers, we examined differential gene expression in each case-control pair separately (Supplementary Fig. 1). All three ARIA+ cases demonstrated concordant upregulation of cytotoxic effector genes, HLA class II molecules, metabolic reprogramming factors, and adhesion/migration genes, alongside downregulation of quiescence markers and tissue residence factors. The consistency of these signatures across radiographically distinct ARIA subtypes (E-only, H-only, and E/H combined) demonstrates that group-level patterns are not driven by outliers and instead may represent broader ARIA-associated changes.

To further explore whether the transcriptional differences identified in ARIA + $CD8^+$ subsets were linked to metabolic regulation, we first inferred transcription factor activity from our scRNA-seq dataset using decoupleR (Fig. 2a). This analysis highlighted shifts in several regulators of T cell metabolism, including consistent downregulation of *VHL* in ARIA + TEM and TEMRA cells. VHL normally constrains hypoxia-inducible factor (HIF) signaling; its reduced activity in ARIA+ effector cells therefore suggests a potential stabilization of HIF-1α and a shift toward glycolytic metabolism, a state known to favor short-lived effector function over long-term persistence[10,11]. Additional TF changes included modulation of PPARA, which regulates fatty acid oxidation, and altered activity of histone deacetylases (HDAC1/3), together indicating broad remodeling of metabolic and epigenetic programs. To validate that reduced VHL activity and inferred HIF1α stabilization correspond to downstream metabolic gene activation, we examined expression of genes with experimentally validated Hypoxia Response Elements (HREs) across CD8 + TEM and TEMRA populations, as well as CD14+ and CD16+ monocyte subsets (Supplementary Fig. 2). ARIA + TEMRA cells showed coordinated upregulation of glycolytic enzymes, alongside downregulation of oxidative phosphorylation (OXPHOS), TCA cycle, and fatty acid oxidation (FAO) genes. This pattern confirms a metabolic shift from oxidative phosphorylation toward aerobic glycolysis consistent with HIF1α-driven transcriptional reprogramming. TEM cells showed similar but less pronounced metabolic signatures, possibly reflecting their intermediate differentiation state. Both CD14+ and CD16+ monocyte subsets displayed parallel metabolic reprogramming in ARIA+ samples, indicating coordinated immunometabolic responses across lymphoid and myeloid compartments (Supplementary Fig. 2).

Immunometabolic reprogramming fuels effector and clonal remodeling

To confirm these transcriptional inferences at the metabolite level, we performed targeted metabolomic profiling of PBMCs from ARIA+ and

https://doi.org/10.1038/s41467-026-68921-3

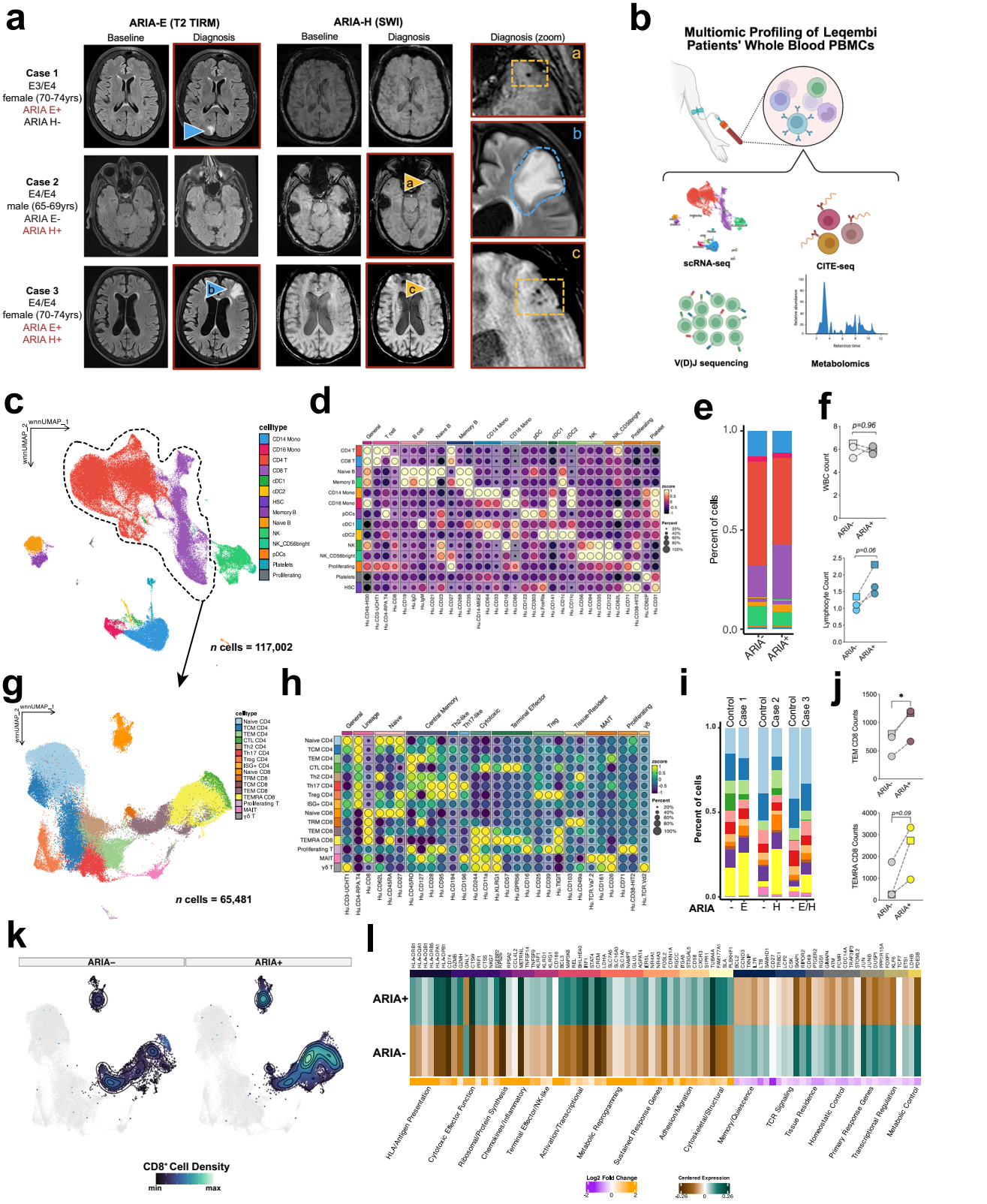

ARIA- patients (Fig. 2b). Principal component analysis revealed a clear separation of ARIA+ from ARIA- samples, demonstrating global differences in metabolite abundance (Fig. 2c, left). This separation was driven by several differentially abundant metabolites in ARIA+ samples, including increases in lactate, pyruvate and itaconate and decreases in citrate, characteristic of the 'broken' TCA cycle observed in pro-inflammatory myeloid cells (Fig. 2c, d)[12]. Pathway impact analysis further supported this observation, identifying enrichment of glycolysis, pyruvate metabolism, and sphingolipid metabolism, alongside perturbations in the TCA cycle and the pentose phosphate pathway (Fig. 2e). These ARIA-driven metabolic shifts are consistent with prior literature establishing a metabolic reprogramming inherent in the regulation of $CD8^+$ effector states and heightened effector activity[13–15].

Fig. 1 | ARIA is associated with expansion of peripheral CD8⁺ TEMRA cells. **a** Representative MRIs show edema/effusions on T2-FLAIR/TIRM (blue triangles) and microhemorrhages/siderosis on SWI (orange triangles) from three selected ARIA cases (ARIA-E, ARIA-H, and ARIA-E/H). Cases were matched to three controls by age, sex, *APOE* genotype, and infusion number. "Baseline" indicates pre-treatment MRI; "At diagnosis" indicates surveillance MRI when ARIA was first detected. Clinical characteristics provided in Supplemental Table 1. **b** Study design and multi-omic profiling workflow (Created in BioRender. Morganti, J. (2026) https://BioRender.com/9hv27wi). PBMCs collected pre-infusion underwent 5′ scRNA-seq with CITE-seq and V(D)J, plus targeted metabolomics. **c**, **d** Multimodal (RNA + Antibody-Derived Tags (ADT)) UMAP of ~117,000 cells resolves major PBMC lineages (T, B, NK, monocytes, DCs). **e** Proportions of major lymphocyte classes show increased CD8⁺ and decreased CD4⁺ frequencies in ARIA+ subjects. **f** Routine clinical counts reveal similar CBC differentials across groups, with a trend toward higher absolute lymphocyte counts in ARIA+ cases. **g**, **h** Re-clustering of 65,481 T cells identifies canonical CD4⁺ (naïve, central/effector memory, Tregs) and CD8⁺ (naïve, central/effector memory, TEMRA, intermediate cytotoxic) states using concordant RNA and surface markers. **i** ARIA+ patients exhibit contraction of naïve CD8⁺ cells and enrichment of effector memory/TEMRA subsets. **j** Quantification of CD8 + TEM and TEMRA absolute cell counts from scRNAseq data. Individual samples show elevations in TEM (top) and TEMRA (bottom) numbers in ARIA+ patients (*p = 0.0234, Student's two-tailed t-Test, squares = male, circles = female). Density plots **k** highlight TEMRA accumulation in ARIA+ only. **l** Differential expression (Fisher meta-analysis) in TEMRA cells from ARIA+ versus ARIA- reveals increased cytotoxic/Fc-receptor signaling, chemokine/migratory genes, MHC-II, inhibitory/stress markers, and metabolic regulators consistent with a glycolytic, glutamine-fueled effector state. Source data are provided as a Source Data file.

Given that glycolytic reprogramming is closely coupled to effector function, we next examined whether ARIA-associated TEM and TEMRA cells also displayed evidence of augmented cytotoxic potential and clonal remodeling. A cytotoxicity module score was lowest in CD4 populations and naïve CD8 cells, but progressively increased in TRM-like, TEM, and TEMRA subsets (Fig. 2f, top). Gene-level summaries demonstrated that cytotoxic mediators rose in a consistent stepwise manner across these states (Fig. 2f, bottom). To capture this trajectory more comprehensively, we applied pseudotime analysis seeded in naïve CD8⁺ cells and terminating in TEMRAs (Fig. 2g). As expected, early stages were characterized by ribosomal and translational genes (*RPL10, RPL32, RPS12, TPT1*), consistent with biosynthetic priming, whereas intermediate states expressed signaling and regulatory molecules including *CCR7, JUNB, ZFP36, DUSP2*, and *IL32*. Terminal effector states were marked by cytotoxic mediators such as *CST7, CTSW, PRF1*, and *GNLY*, together with effector-associated receptors (*KLRG1, FCRL6*) and persistence factors (*LGALS1, EFHD2*). The associated pathways reflected this continuum, beginning with lymphoid development and antigen processing and culminating in granzyme-mediated cytotoxicity and programmed cell death (Fig. 2g, right).

It has been well established that clonal expansion occurs in parallel with differentiation into effector and memory subsets[10,11]. To test this, we assessed clonal architecture using V(D)J sequencing. ARIA+ patients harbored a greater burden of expanded clones than ARIA- controls, with an over-representation of medium and large clones (Fig. 2h). Linking transcriptomes to clonal size showed that larger CD8⁺ clones were increasingly enriched for effector–cytotoxic programs, including *GZMB/GZMH/GNLY* and the chemokine *CCL4*[16]. Regulators (*EOMES*, *LYN*)[17,18], NK/cytotoxic receptors (*KLRC2, CMKLR1, SIGLEC17P*), and antigen-presentation/adhesion genes (*HLA-DQA1, ITGAM)* were also elevated, and pathway analysis confirmed progressive enrichment for cell-killing functions with clonal expansion.

Integration of transcriptional data with clone size demonstrated that larger clones were enriched for effector and cytotoxic gene programs (Fig. 2i). Prominent among these were granzymes B and H (*GZMB, GZMH*) and granulysin (*GNLY*), which mediate perforin-dependent lysis of target cells[16]. The chemokine CCL4, a CCR5 ligand that promotes recruitment of leukocytes to inflamed tissues, was also increased[19]. Transcriptional regulators including EOMES and the Src-family kinase LYN were enriched, consistent with effector CD8 differentiation and TCR signaling modulation[17,18], and expanded clones expressed cytotoxic or NK-associated receptors (*KLRC2, CMKLR1, SIGLEC17P*) and molecules linked to antigen presentation and adhesion (*HLA-DQA1, ITGAM*). Pathway analysis aligned with these observations, showing that larger clones were increasingly enriched for programs involved in cell killing and cytotoxic effector function (Fig. 2i, right).

Together these data show that ARIA+ patients exhibit remodeling of the CD8 compartment across multiple axes. Naïve cells remain unchanged in frequency and clonality, TRM-like cells maintain stable numbers but undergo selective clonal expansion, and both TEM and TEMRA subsets expand in number and clonality while acquiring progressively stronger cytotoxic programs. These findings mirror prior reports that clonally expanded CD8⁺ TEMRAs patrol the CSF in AD, enriched for cytotoxic effectors and in some cases specific for viral antigens[20]. Similar patterns of antigen-driven clonal expansion have been described in CMV infection[21], multiple sclerosis[22], and aging-related immunosenescence[23], supporting the conclusion that ARIA is associated with both numerical and clonal reshaping of antigen-experienced, high-effector capacity CD8⁺ subsets. In this context, ARIA appears to reflect a coordinated metabolic, cytotoxic, and clonal reshaping of the effector CD8⁺ pool, positioning these cells for vascular engagement and potential endothelial injury.

Monocyte signaling and vascular 'homing' link CD8⁺ effectors to ARIA pathology

While these features define the intrinsic state of TEM and TEMRA cells, they raise the question of what extrinsic cues initiate and sustain such reprogramming. Because T cell differentiation and cytotoxic potential are strongly influenced by cell:cell signaling within the peripheral immune compartment, and because ARIA pathology manifests at the vascular interface, we asked if altered intercellular communication underlies these expanded TEM and TEMRA cells. To this end, GSEA analysis revealed differential (ARIA+ vs. ARIA-) enrichment of multiple terms analysis across the CD8⁺ subtypes (Fig. 3a). Pathway enrichment clustered around immune interfaces (chemotaxis, lymphocyte activation, interferon signaling, antigen presentation), vascular interfaces (BBB transport, endothelial activation, integrins, vessel morphogenesis), and neural context (APP catabolism), indicating ARIA-associated TEMRA states potentially linked to cerebrovascular injury and amyloid response.

To investigate whether altered intercellular communication contributes to the expansion and effector reprogramming of CD8⁺ subsets in ARIA, we next examined ligand–receptor interactions between CD14⁺ or CD16⁺ monocytes and CD8⁺ T cells. Prior work has shown that monocytes can upregulate MHC molecules and co-stimulatory ligands, thereby shaping T-cell activation and differentiation[24,25]. Comparing CD14⁺ and CD16⁺ monocytes revealed marked transcriptional differences that were exaggerated in ARIA+ samples (Fig. 3b). CD14⁺ monocytes showed enrichment for pathways linked to type I interferon signaling, antigen presentation, and leukocyte adhesion, while CD16⁺ monocytes preferentially expressed transcripts involved in vascular interactions, extracellular matrix remodeling, and cell killing.

Network-level analyses highlighted that TEM and TEMRA cells received most incoming signals from CD14⁺/CD16⁺ monocytes in ARIA + samples. Chord and dot plots revealed several recurrent ligand-receptor axes, including HLA class II-CD4/TCR interactions reflecting monocyte antigen presentation to CD8⁺ cells[26], ICAM1-LFA1 and CD58-CD2 adhesion axes that stabilize immune synapses[27], and chemokine signaling (CCL3/4-CCR5, CXCL10-CXCR3)[28] pathways previously implicated in vascular homing and effector cell recruitment (Fig. 3c, d).

https://doi.org/10.1038/s41467-026-68921-3

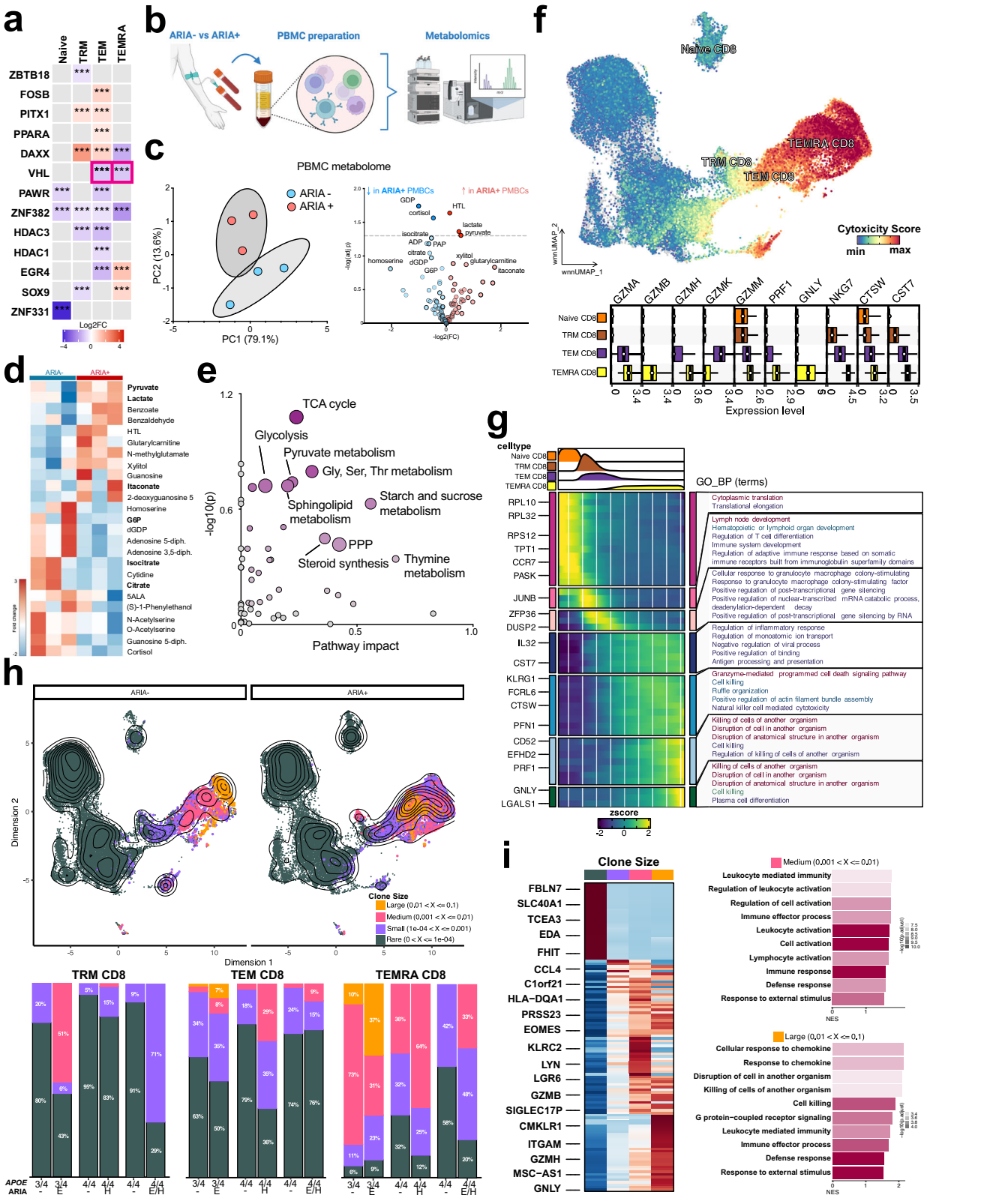

Together these results indicate that ARIA+ monocytes not only present antigen but also create an adhesive and chemokine-rich milieu that preferentially engages TEM/TEMRAs.

Since our dataset comprises peripheral blood only, we leveraged a complementary brain single-nucleus resource to ask whether blood-derived CD8 programs mirror vascular-interacting states. Using the lecanemab (LCMB) dataset from van Olst et al.[9], we projected our CD8$^+$ subsets into an endothelial-interaction framework (Fig. 3e).This analysis revealed that TEM and TEMRA cells established an in silico connectivity to brain endothelial clusters, through adhesion and chemokine receptor pathways similar to those identified in our monocyte analyses (ICAM1-ITGAL/ITGB2, VCAM1-ITGA4/ITGB1, CXCL10-CXCR3). Chord diagrams illustrated that ARIA+ samples showed broader and stronger inferred interactions across endothelial

Fig. 2 | ARIA is associated with immunometabolic reprogramming, increased cytotoxicity, and clonal remodeling of CD8⁺ T cells. a Transcription factor activity inferred with decoupleR shows reduced VHL activity (red boxes) in ARIA + TEM/TEMRA cells. Activity scores compared between ARIA+ and ARIA− within each cell type; $n = 3$ biologically independent patients per group; differential activity assessed by two-tailed t-test with Benjamini-Hochberg correction; significance defined as adjusted $p < 0.05$ and $|\log_2 FC| > 0.5$. **b** Targeted PBMC metabolomics workflow (Created in BioRender. Johnson, L. (2026) https://BioRender.com/09ib3if). **c**, **d** Principal component analysis of metabolomic profiles from $n = 3$ ARIA+ and $n = 3$ ARIA− biologically independent patient samples (one measurement per patient), Volcano plot showing differential metabolite abundance; two-tailed t-test with Benjamini-Hochberg correction; metabolites with $p < 0.05$ and $|\log_2 FC| > 0.5$ labeled. Heatmap highlights individual metabolites across samples showing increased lactate, pyruvate, and itaconate with decreased citrate in ARIA + . **e** Pathway impact analysis using MetaboAnalyst; enrichment assessed by hypergeometric test with Benjamini-Hochberg correction; pathway impact calculated by topological analysis, hypergeometric test (one-tailed, testing for over-representation) with Benjamini-Hochberg correction for multiple comparisons. **f** Cytotoxicity module scores across CD8+ subsets. Box plots show median (center line), interquartile range (box bounds), and whiskers extending to 1.5x IQR. Cell numbers per subset: Naive CD8 ($n = 3{,}085$ cells), TRM CD8 ($n = 892$ cells), TEM CD8 ($n = 4{,}967$ cells), TEMRA CD8 ($n = 9{,}262$ cells) across 6 biologically independent patients; Wilcoxon rank-sum test comparing adjacent differentiation states. **g** Pseudotime trajectory from naïve CD8⁺ to TEMRA inferred using Slingshot; 200 variable genes shown. **h** Clonal expansion categories by V(D)J sequencing. Left: proportion of clones by expansion category for each patient ($n = 3$ ARIA + , $n = 3$ ARIA − ; biologically independent). Right: subset-specific clonality compared between groups. **i** Differential expression by clone size; Wilcoxon rank-sum test comparing clonal categories; genes with adjusted $p < 0.05$ and $\log_2 FC > 1$ shown; Gene Ontology enrichment by two-tailed hypergeometric test with Benjamini-Hochberg correction. Source data are provided as a Source Data file.

subtypes (Fig. 3f), reinforcing the view that these effector subsets are transcriptionally primed for vascular engagement.

Summarizing these signals, TEMRAs accounted for most predicted cerebrovascular interactions, followed by TEM and TRM-like cells, with naïve cells contributing minimally (Fig. 3g). Beyond their cytotoxic program, TEMRAs also carry the chemotaxis/adhesion repertoire that favors vascular engagement (for example, CCR5/CXCR3/CX3CR1, ITGAL/ITGB2, ITGA4/ITGB1, and CD2–CD58/ICAM1–LFA-1), which our monocyte→T-cell analyses and in silico endothelial mapping both prioritize. When we integrate these signatures with the cerebrovascular and Aβ-niche context reported in the van Olst study[9], our data support a model in which peripheral TEM/TEMRAs are transcriptionally "addressed" to the diseased vascular interface and plausibly traffic into affected tissue under inflammatory conditions.

Discussion

This case-control study identifies a coordinated peripheral immune program associated with ARIA during lecanemab treatment. Across multiple data modalities, we observed expansion of CD8 + TEM and TEMRA subsets with metabolic reprogramming toward glycolysis, increased clonal burden, and enhanced cytotoxic programming. These intrinsic features were coupled with altered monocyte-T cell communication axes and transcriptional signatures aligned with cerebrovascular engagement. Together, these findings reveal peripheral immune changes that associate with ARIA and may inform biomarker development for risk stratification. While the cross-sectional design precludes causal inference, the convergent findings across multiple data modalities establish this as a hypothesis-generating resource for understanding ARIA pathophysiology.

The expansion of CD8⁺ TEMRA cells in ARIA+ patients extends emerging evidence linking CD8+ populations to AD pathology[29–31]. Gate et al.[20] identified clonally expanded CD8+ TEMRAs patrolling the CSF in AD, enriched for cytotoxic effectors and, in some cases, harboring specificity for viral antigens. Our findings parallel this observation and demonstrate that similar changes are peripherally detectable and associate with treatment-emergent vascular pathology; though whether peripheral and CNS TEMRA populations represent the same clones or parallel expansions remains to be determined. The transcriptional features we observed—high expression of granzymes, perforin, and granulysin alongside inhibitory receptors and stress markers—align with established TEMRA biology in aging and chronic inflammation[32,33]. This dual program of potent cytotoxicity and partial exhaustion is consistent with chronic antigenic stimulation, as described in the "inflammaging" hypothesis where persistent low-grade inflammation drives terminal differentiation[34]. Whether ARIA represents an amplification of age-related TEMRA accumulation or reflects a qualitatively distinct activation state cannot be determined from our cross-sectional comparison; however, the metabolic reprogramming and clonal expansion patterns we observe would seem to suggest active immune processes rather than simply passive age-related accumulation.

The expression of MHC class II molecules on ARIA+ TEMRAs warrants consideration. While CD8 + T cells classically recognize MHC class I, MHC-II expression has been documented in chronic inflammatory settings through two mechanisms: direct transcriptional upregulation in response to inflammatory signals, or acquisition from antigen-presenting cells via trogocytosis[26,35]. Recent work has shown that HLA-DR⁺ CD8⁺ T cells correlate with disease severity with enhanced effector functions[36,37]. In our ARIA context, this may reflect heightened activation state or increased interaction with professional antigen-presenting cells (APCs), particularly given the concurrent upregulation of antigen presentation pathways in monocytes, which is in line with prior reports of lymphocyte:monocyte cross-talk at the CNS borders[24,38]. It is important to consider whether the MHC-II expression on ARIA-associated TEMRAs is functionally significant or represents a marker of activation state; this will require functional studies examining antigen presentation capacity and T-T cell interactions.

Similar CD8 + TEMRA expansions occur in other neuroinflammatory conditions including multiple sclerosis, where tissue-resident memory populations localize to perivascular and meningeal regions and undergo clonal expansion. This raises the question of whether our findings reflect ARIA-specific biology or a general vascular inflammatory response. Several features suggest contextual specificity: (1) the temporal association with lecanemab treatment and Aβ immune complex formation; (2) the monocyte activation signature consistent with Fc-receptor engagement; (3) the correlation with *APOE4* genotype, which may influence both amyloid deposition *and* immune responses. However, shared mechanisms between ARIA and other cerebrovascular inflammatory processes likely exist, and comparative studies with MS and other vascular disorders would clarify disease-specific versus common pathways.

Importantly, similar CD8⁺ expansions characterize other CNS pathologies with vascular involvement. In multiple sclerosis, TEMRA and tissue-resident memory populations localize to perivascular and meningeal regions, where they undergo clonal expansion and contribute to lesion formation[22,39,40]. Experimental models further demonstrate that activated CD8⁺ cells localize to, and can directly injure, vascular endothelium through perforin-dependent mechanisms, leading to blood-brain barrier (BBB) disruption[41,42]. These precedents support a model where expanded peripheral TEMRAs in ARIA + patients could similarly engage and damage cerebral vasculature. The metabolic shift toward glycolysis in ARIA + CD8⁺ cells provides mechanistic insight into their functional state. Our transcription factor inference revealed downregulation of VHL, the E3 ubiquitin ligase that

https://doi.org/10.1038/s41467-026-68921-3

targets HIF-1α for degradation. Loss of VHL function stabilizes HIF-1α, driving metabolic reprogramming from oxidative phosphorylation to aerobic glycolysis, a well-characterized phenomenon in effector T cells[43]. This metabolic state, while less efficient for ATP generation, provides rapid energy and biosynthetic precursors necessary for effector functions including cytokine production, proliferation, and cytotoxic granule synthesis[44,45]. Recent community-based work by Winford et al further supports this framework by showing that peripheral CD8⁺ TEMRAs correlate with plasma markers of neuronal injury (Nf-L) and vascular:astrocytic disruption (GFAP), even in the absence of AD-specific biomarker changes[46]. While their study did not link CD8⁺ TEMRAs to cognition or amyloid pathology, the alignment of TEMRA frequency with injury markers suggests that these cells may act as sentinels of tissue damage. Our findings extend this concept to the

Fig. 3 | ARIA reshapes monocyte–T-cell communication and primes effector CD8⁺ subsets for cerebrovascular engagement. a Gene set enrichment analysis comparing ARIA+ versus ARIA− across CD8 subsets; $n = 3$ biologically independent patients per group; enrichment assessed by two-tailed permutation test (1000 permutations) with Benjamini-Hochberg correction; gene sets with adjusted $p < 0.05$ shown. **b** Monocyte transcriptional programs comparing CD14⁺ and CD16⁺ subsets between ARIA+ and ARIA− samples. **c** Cell-cell communication strength (CellChat) showing incoming signals to CD8 subsets from monocytes; communication probabilities calculated per condition (ARIA+ or ARIA −) with n = 3 biologically independent patients per group (Created in BioRender. Morganti, J. (2026) https://BioRender.com/oqzqxjb). **d** Ligand-receptor interaction dot plot; dot size indicates communication probability; color indicates pathway. **e** Cross-modal integration with brain endothelial cells from van Olst et al.[9]; peripheral CD8 subsets from this study ($n = 3$ ARIA+ patients) projected onto endothelial interaction framework (Created in BioRender. Morganti, J. (2026) https://BioRender.com/oqzqxjb). **f** Chord diagrams showing inferred endothelial interactions; line thickness proportional to interaction strength. **g** Proportion of predicted cerebrovascular interactions by CD8 subset.

vascular domain, demonstrating that CD8⁺ TEMRAs expand specifically in the setting of treatment-emergent vascular injury during ARIA, though whether this represents cause or consequence cannot be determined from our cross-sectional design.

The metabolomic validation showing elevated lactate and pyruvate with reduced TCA cycle intermediates confirms active glycolytic flux. This pattern mirrors the metabolic signature of short-lived effector cells, which prioritize immediate function over long-term survival[47]. Scharping et al.[48] demonstrated that sustained glycolysis in CD8+ cells correlates with enhanced cytotoxicity but reduced persistence, potentially explaining why ARIA+ TEMRAs express both effector molecules and exhaustion markers. This metabolic reprogramming likely represents both cause and consequence of effector differentiation. Along similar lines, Cheng et al.[13] showed that enforcing glycolysis drives CD8+ cells toward effector fates, while blocking glycolysis promotes memory formation. In the ARIA context, the combination of antigenic stimulation (likely from Aβ-antibody complexes) and inflammatory signals from activated monocytes may create a feed-forward loop where metabolic reprogramming sustains effector expansion and function, although again, the directionality of these relationships remains to be established.

The increased clonal burden in ARIA+ patients, particularly within TEM and TEMRA compartments, indicates antigen-driven proliferation. The correlation between clone size and cytotoxic gene expression follows established principles where TCR stimulation strength determines both proliferative capacity and effector differentiation[10,11]. The enrichment of EOMES and TBX21 in expanded clones aligns with their roles as master regulators of CD8+ effector differentiation[17]. The pattern of clonal expansion, minimal in naïve cells, selective in TRM-like cells, and pronounced in TEM/TEMRA, is consistent with progressive selection during differentiation. This mirrors observations in chronic viral infections, where CMV-specific CD8⁺ cells can comprise >10% of the total CD8⁺ pool and exhibit similar TEMRA phenotypes[21]. In aging-related immunosenescence, such clonal expansions correlate with reduced immune diversity and increased susceptibility to novel pathogens[23]. Whether ARIA-associated clones recognize Aβ epitopes, vascular antigens, or latent viral antigens reactivated during inflammation remains to be determined through TCR sequencing and antigen specificity testing.

The altered monocyte-T cell signaling in ARIA+ samples provides the extrinsic cues necessary for CD8⁺ activation and trafficking. The upregulation of adhesion molecules (ICAM1, VCAM1) and chemokines (CCL3/4, CXCL10) by ARIA+ monocytes creates a milieu that would favor T cell recruitment and activation. These molecules can mediate the classical adhesion cascade whereby circulating lymphocytes undergo selectin-mediated rolling, chemokine-triggered activation, integrin-dependent firm adhesion, and ultimately transmigration[27,49]. The specific chemokine-receptor pairs we identified, CCL3/4-CCR5 and CXCL10-CXCR3, have established roles in neuroinflammation. CCR5⁺ T cells preferentially traffic to inflamed CNS in multiple sclerosis and HIV encephalitis[19], while CXCR3 engagement promotes T cell migration across the BBB in response to IFN-γ-induced CXCL10 production by astrocytes and endothelial cells[50]. The concurrent expression of LFA-1 and VLA-4 on ARIA+ TEMRAs provides the integrin repertoire that could facilitate firm adhesion to activated endothelium expressing ICAM1 and VCAM1.

Our in silico mapping to the van Olst et al.[9] cerebrovascular atlas provides spatial CNS context for these peripheral findings. That study demonstrated microglial activation, complement deposition, and endothelial changes at sites of Aβ clearance following immunization. Our data suggest that circulating TEMRAs are transcriptionally expressing potential coordinated programs to engage these activated vascular niches through matching adhesion and chemokine programs. The stronger predicted interactions in ARIA+ samples are consistent with enhanced capacity for vascular engagement, potentially tipping the balance from successful Aβ clearance to pathological vascular injury. Whether these concordant expression profiles represent cause or consequence of ARIA cannot be casually established from our current study design. However, we propose a working model in which ARIA may reflect coordinated peripheral and central immune activation. In this model, systemic antibody administration triggers Aβ mobilization and immune complex formation, activating both circulating monocytes and CNS-resident microglia. The resulting chemokine gradients and adhesion molecule upregulation could create conditions that recruit glycolytically reprogrammed, clonally expanded TEMRAs. These cells, expressing cytotoxic machinery and effector programs, might then interact with cerebral vasculature. However, this model remains speculative and requires validation through longitudinal studies, functional assays, and experimental models. Alternative explanations, including that immune changes are reactive rather than causative, cannot be excluded based on our cross-sectional observations.

The relationship between cardiovascular risk factors and ARIA in our cohort suggests a complex, multifactorial etiology. While all ARIA+ patients had at least one cardiovascular risk factor compared to only one control, the absence of dose-response relationship indicates that vascular comorbidities alone cannot explain ARIA susceptibility. Patient 5, with concurrent hypertension and hyperlipidemia, did not develop ARIA despite having cardiovascular burden and E4/E4 homozygosity. Conversely, Patients 2 and 6 developed ARIA with hyperlipidemia only. These patterns suggest that cardiovascular risk factors may create permissive conditions for ARIA but that additional immune-mediated mechanisms, specifically the CD8 + TEMRA expansion and metabolic reprogramming we identified, may differentiate which individuals progress to radiographic abnormalities. This hypothesis predicts that immune signatures will provide more specific risk stratification than cardiovascular profiles alone and warrants validation in larger cohorts combining vascular and immunological biomarkers.

Our findings have potential implications for ARIA risk assessment and mitigation. The peripheral signature we identified – TEMRA expansion, metabolic shift, and clonal skewing – could form the basis for a pre-treatment screening panel, warranting future experiments incorporating longitudinal sampling. Patients with elevated baseline TEMRA frequencies or glycolytic signatures might warrant modified dosing schedules or enhanced monitoring. Serial assessment during early infusions could identify evolving risk before radiographic ARIA appears, though whether such changes predict radiographic ARIA or simply correlate with it remains to be determined in longitudinal studies.

If the immune changes we identify are validated as causative rather than reactive, therapeutic interventions could be considered. Transient metabolic modulation to reduce glycolysis during initial antibody doses might limit TEMRA expansion without compromising long-term treatment efficacy. Alternatively, temporary blockade of specific adhesion molecules (anti-VLA4, as used in natalizumab for MS) or chemokine receptors (CCR5 antagonists) during peak risk periods could reduce CNS trafficking while preserving peripheral immunity. The timing would be critical; intervention should coincide with early Aβ mobilization but not persist long enough to impair beneficial microglial clearance mechanisms.

Several important caveats should be considered when interpreting these findings. Most critically, our associations may reflect cause, consequence, or correlated response to ARIA. The $CD8^+$ TEMRA expansion and metabolic reprogramming we observe could represent a causal driver of vascular injury through direct endothelial damage, a consequence of cerebrovascular damage with subsequent peripheral immune activation, or a parallel response to immune complex formation where both vascular injury and T cell activation are downstream of antibody-Aβ interactions. The sample size of three matched pairs, while enabling deep multi-omic characterization, limits statistical power and precludes definitive mechanistic conclusions or assessment of APOE genotype-specific effects despite ε4 carriage being the strongest known risk factor for ARIA. Additionally, our analysis relies exclusively on peripheral blood, which may not fully reflect CNS immune events, and the integration with cerebrovascular data from van Olst et al. uses an external dataset from a different cohort, requiring cautious interpretation of inferred peripheral-to-brain trafficking patterns. The matched case-control design, while controlling for major confounders, cannot account for all variables that might influence immune profiles, including subclinical infections, medication history, or genetic factors beyond APOE, and the heterogeneity of ARIA presentation in our cohort prevents subset-specific analyses.

These limitations point directly to critical next steps. Temporal profiling across the infusion timeline would establish the kinetics of immune changes relative to ARIA onset and determine whether changes precede or follow radiographic abnormalities, a prerequisite for distinguishing among causal interpretations. A larger cohort stratified by APOE genotype would enable robust statistical analysis and identification of genotype-specific risk factors. Functional validation through ex vivo cytotoxicity assays, endothelial co-cultures, and chemotaxis experiments would determine whether ARIA-associated TEMRAs are capable of vascular damage. TCR sequencing paired with epitope mapping could identify the antigens driving clonal expansion, whether Aβ epitopes, vascular proteins, viral antigens, or neo-epitopes, addressing current uncertainty about bystander versus antigen-specific activation. Experimental models in which specific immune components are manipulated would be required to establish causality. Finally, if predictive value is demonstrated, development of a simplified clinical assay focusing on key markers (e.g., TEMRA frequency, metabolic ratios, selected chemokines) would enable prospective validation and eventual clinical implementation.

In summary, we describe a coordinated peripheral immune program associated with ARIA during lecanemab treatment, characterized by metabolic reprogramming, clonal expansion, and altered intercellular communication in CD8+ effector populations. While the cross-sectional design and small sample size preclude causal inference, the convergent findings across multiple data modalities provide biological insights into immune changes accompanying ARIA and establish a foundation for hypothesis testing in larger, longitudinal cohorts. As anti-amyloid therapies become standard care, determining whether peripheral immune signatures can predict ARIA risk and whether immune modulation can safely reduce ARIA incidence will be critical questions for the field.

Methods

Participant identification and recruitment

Study participants were identified and consented by Norton Neuroscience Institute Memory Clinic staff members. Informed consent was collected under an existing IRB protocol (University of Louisville Institutional Review Board, #42.007). Study participants were matched by sex, *APOE* genotype, ARIA status, and infusion number. Participants consented to their samples being used in this study and were not compensated for study participation.

Blood collection and processing

Blood was collected immediately prior to lecanemab infusion in BD Vacutainer EDTA-coated tubes. After collection, blood was handed off to UK staff to be transported in biohazard containers to UK labs. PBMC and plasma isolation was done using density gradient centrifugation using SepMate tubes. 5 mL of plasma was removed from the top layer of the tube for use in metabolomics and biomarker assays. PBMC layer was further processed with an additional wash and RBC lysis before counting and resuspension in freezing media (90% Fetal bovine Serum (VWR), 10% Dimethylsulfoxide (Invitrogen)). Cells were then allowed to cool to −80C overnight in a slow cooler (Nalgene Mr. Frosty) before transfer to LN2 for long term storage.

Thawing and Counting of Cells

Cells were removed quickly from LN2 and immediately placed on dry ice for transfer to a 37 C water bath. Cells were monitored while thawing, and when ~90% thawed quickly decanted into pre-warmed RPMI-1640 media (Gibco) supplemented with 10% FBS and 1% Penicillin-Streptomycin cocktail. Cells were pelleted and resuspended in 1 mL of DPBS supplemented with 2% FBS for counting and downstream applications. Cell counting was conducted using a hemacytometer at a dilution factor of 1:5 in Trypan Blue. Manual cell counts were verified with Denovix Cell counter.

Sample collection and single-cell library preparation

PBMCs were isolated from six patients (Supplemental Table 1) and processed using 10x Genomics Chromium Single Cell 5′ chemistry. Simultaneous capture of transcriptomic and surface protein expression was achieved using TotalSeq-C antibody-derived tags (ADTs) targeting 137 surface proteins. T cell receptor sequences were captured using 10x Genomics V(D)J enrichment. Libraries were sequenced on an Illumina NovaSeq 6000 system and processed using Cell Ranger multi v9.0.1 to generate filtered feature-barcode matrices.

Metabolomics

Targeted metabolomic profiling was performed on PBMC samples (n = 3 ARIA +, n = 3 ARIA −; one sample per patient, no technical replicates). Cells (1×10^6 per sample) were pelleted, rinsed with ice-cold DPBS, and quenched with 1 mL ice-cold 50% HPLC-grade methanol followed by incubation at −80 °C for 10 min. Samples were homogenized using a Disruptor Genie (Scientific Industries) at 3,000 rpm for 5 min, centrifuged at 20,000 × g for 10 min at 4 °C, and supernatants stored at −80 °C until analysis.

Metabolite separation was performed on an Agilent InfinityLab Poroshell 120 EC-C8 column (150 × 2.1 mm, 2.7 μm) using an Agilent 1290 Infinity II LC system. Mobile phase consisted of 15% water/85% acetonitrile with 10 mM ammonium acetate and 2.5 μM InfinityLab Deactivator Additive (pH 9). The gradient program at 0.4 mL/min was: 0 min, 90% B; 1 min, 90% B; 8 min, 78% B; 12 min, 60% B; 15 min, 10% B; 18 min, 10% B; 19 min, 90% B; 23 min, 90% B. Mass spectrometry was performed on an Agilent 6495D triple quadrupole (QQQ) system using dynamic multiple reaction monitoring (dMRM) with polarity switching. Data acquisition and processing were performed using Agilent MassHunter Workstation software (version 12.1). Blanks were run before and after sample sequences; two quality control samples

(pooled) were run in parallel with experimental samples. Volcano plots, heatmaps, and pathway enrichment analysis were performed using MetaboAnalyst 5.0.

Quality control and data preprocessing

Individual Seurat objects were created using Seurat v5.3.0 with filtering criteria of ≥200 detected genes per cell and ≥3 cells per gene. Quality control metrics were calculated for mitochondrial, ribosomal, and hemoglobin gene content. Cells exceeding 10% mitochondrial gene expression were excluded. Putative doublets were identified and removed using scDblFinder v1.20.2, and ambient RNA contamination was corrected using decontX v1.4.1. After quality control, the dataset comprised 116,669 immune cells across 6 samples.

Multimodal data integration and dimensionality reduction

RNA data were normalized using SCTransform with mitochondrial percentage regression, excluding ribosomal genes from variable feature selection. Data were split by sample and the top 3,000 variable genes were selected. Principal component analysis was performed retaining the first 50 components. ADT data were normalized using centered log-ratio transformation followed by scaling. All 137 ADT features were used as variable features with principal component analysis retaining the first 30 components. Cross-sample integration was performed using reciprocal principal component analysis independently for RNA and ADT modalities. The integrated representations were combined using weighted nearest neighbor analysis to generate a unified multimodal embedding. Graph-based clustering was performed on the WNN graph using the Leiden algorithm (resolution = 1.0). UMAP visualization was computed using the WNN embedding.

Cell type annotation and classification

Major immune populations were identified using surface protein (ADT) markers with RNA expression used for additional subset refinement. T cells were identified by CD3+ and CD3E + ; B cells by CD19+ and MS4A1 + ; classical monocytes by CD14+ (CD14 + , LYZ +) and non-classical monocytes by CD16+ (FCGR3A + , CX3CR1 +); NK cells by CD56+ and NCAM1 + ; and dendritic cells by CD123+ (pDCs), CD141+ (cDC1), or CD1c+ (cDC2) with corresponding RNA markers CLEC4C + , CLEC9A + , or CD1C + . Additional populations included naive B cells (IgD + , CD23 + ; IGHD + , FCER2 +), memory B cells (CD27 + ; TNFRSF13B +), conventional NK cells (CD56 + , CD16 + ; NCAM1 + , NKG7 +), CD56bright NK cells (CD56 + , CD122 + ; IL7R + , SELL +), proliferating cells (CD71 + ; MKI67 +), platelets (CD62P + ; PPBP + , PF4 +), and hematopoietic stem cells (CD34 + ; KIT +). Contaminating clusters were excluded prior to downstream analysis.

T lymphocytes (65,481 cells) were subset and re-integrated using identical parameters (resolution = 0.8) for fine-grained classification. CD4 + T cell subsets included naive (CD45RA + , CD62L + ; CCR7 + , SELL +), central memory (CD45RO + , CD127 + ; IL7R + , BCL2 +), effector memory (CD45RO + ; GZMK +), cytotoxic (GZMB + ; GZMA + , PRF1 +), Th2 (CD194 + ; GATA3 +), Th17 (CD196 + ; CCR6 +), regulatory (CD25 + , TIGIT + ; FOXP3 + , IL2RA +), and interferon-stimulated (IFI44L + , IFIT1 + , OAS1 +). CD8 + T cell subsets included naive (CD45RA + , CD62L + ; CCR7 + , SELL +), effector memory (CD45RO + ; GZMA + , CCL5 +), terminally differentiated effector memory (TEMRA; CD45RA + , KLRG1 + ; GNLY + , GZMB +), and tissue-resident memory (CD103 + ; ITGAE + , CD69 +). Additional T cell populations included proliferating T cells (CD71 + ; MKI67 +), mucosal-associated invariant T cells (TCR Vα7.2 + ; TRAV1-2 + , KLRB1 +), and γδ T cells (TCR Vδ2 + ; TRDV2 + , TRGV9 +).

TCR sequence analysis and clonal reconstruction

TCR contigs were processed using scRepertoire v2.3.4. Clonotypes were defined by identical CDR3 amino acid sequences for both α and β chains. Clonal expansion was quantified within samples and categorized by relative frequency: Rare ($\leq 10^{-4}$), Small (10^{-4} to 10^{-3}), Medium (10^{-3} to 10^{-2}), Large (10^{-2} to 10^{-1}), and Hyperexpanded ($>10^{-1}$). TCR data were integrated with gene expression profiles, and repertoire diversity, V(D)J gene usage, and clonal overlap analyses were performed.

Differential expression analysis

Cell type-specific differential expression analysis used Wilcoxon rank-sum tests via Seurat's FindMarkers function. Pairwise comparisons were made between ARIA+ and ARIA− samples matched by APOE genotype and sex (minimum 10% expression threshold). Fisher's method was employed for meta-analysis across pairwise comparisons using the test statistic $\chi^2 = -2\Sigma\ln(pi)$. Only genes detected in ≥2 independent comparisons were included. Genes were considered significantly differentially expressed with meta-analysis adjusted p-value < 0.001 (FDR) and absolute mean log fold-change >0.25. Analysis was performed separately for RNA and protein expression data.

Clonal expansion differential expression analysis

Differential expression across T cell clonal expansion states used SCP's RunDEtest function with Wilcoxon rank-sum tests. Clonal categories (Rare, Small, Medium, Large) were compared using log fold-change threshold >1 and adjusted p-value < 0.05, focusing on upregulated genes. Gene Ontology enrichment analysis was performed on clone size-specific differentially expressed genes using biological process terms, with Gene Set Enrichment Analysis to identify pathways associated with clonal expansion states.

Pathway enrichment analysis

Gene Ontology enrichment analysis was performed using clusterProfiler v4.14.6 with org.Hs.eg.db annotation. Biological process terms were tested using over-representation analysis with Benjamini-Hochberg correction (p-value cutoff 0.05, q-value cutoff 0.2). Gene Set Enrichment Analysis was performed on pre-ranked gene lists using gseGO (minimum gene set size 10, maximum 500, p-value cutoff 0.05).

Cytotoxic potential scoring

Cytotoxic capacity was quantified using AUCell v1.28.0 with a curated gene signature (*GZMA, GZMB, GZMH, GZMK, GZMM, PRF1, GNLY, NKG7, CTSW, CST7*). Area under the curve scores were computed using the top 5% of ranked genes per cell and compared across CD8 + T cell subsets.

Cell-cell communication inference

Intercellular communication networks were reconstructed using CellChat v2.2.0 with the CellChatDB.human ligand-receptor database. Analysis was performed separately for ARIA+ and ARIA− conditions. Communication probabilities were calculated for each ligand-receptor pair between cell type pairs, with filtering requiring ≥10 cells per group. Pathway-level communication strengths were aggregated and compared between conditions.

Pseudotime trajectory inference

CD8 + T cell differentiation trajectories were reconstructed using Slingshot v2.14.0 implemented through SCP v0.5.6. Lineages were inferred in the integrated low-dimensional space using cell type annotations as constraints. Dynamic gene expression patterns were identified along pseudotime using 200 highly variable genes.

Gene regulatory network analysis

Cell type-specific gene regulatory networks were constructed using CellOracle v0.20.0 with the human promoter-based reference network from the CellOracle database. After random downsampling to 20,000 cells, principal component analysis was performed with automatic selection of informative components. K-nearest neighbor imputation

was applied (k = 2.5% of total cells) with balanced sampling. Cell type-specific networks were constructed (α = 10) and predictive models fitted for perturbation simulation. Gene knockout simulations were performed by setting target expression to zero with 3 propagation steps. Vector field analysis used 200 nearest neighbors for transition probability estimation.

Transcription factor activity analysis

Transcription factor activities were inferred using decoupleR v2.12.0 with the CollecTRI network obtained via get_collectri(). The Univariate Linear Model (ULM) method was applied to SCT-normalized expression data to estimate transcription factor activities based on target gene expression with minimum regulon size of 5 genes. Differential transcription factor activity analysis was performed within each cell type using t-tests comparing ARIA+ vs ARIA− samples, with a pseudocount of 2 added before log2 fold-change calculation. Results were adjusted for multiple testing using the Benjamini-Hochberg method, with significance defined as adjusted p-value < 0.05 and absolute log fold-change >0.5. Transcription factors were clustered using Ward's hierarchical clustering based on activity patterns across cell types.

Metabolic pathway analysis

Metabolic reprogramming in CD8 + T cell subsets was assessed using selected genes from MSigDB Hallmark pathways, supplemented with additional curated genes for lactate metabolism, TCA cycle, fatty acid oxidation, and mitochondrial biogenesis. Expression data were visualized using dot plots showing mean expression, percent of cells expressing, and statistical significance determined by Wilcoxon rank-sum tests comparing ARIA+ vs ARIA− within each CD8+ subset.

Intercellular communication network analysis

Cell-cell communication networks were analyzed using complementary approaches. For monocyte-CD8 + T cell communication within ARIA samples, MultiNicheNet v2.1.0 and CellChat v2.2.0 analyses were performed. MultiNicheNet analysis used ligand-receptor networks and regulatory matrices from the MultiNicheNet database (human v30112033). Cell type filtering required ≥10 cells per group, gene filtering used minimum sample proportion of 0.50 and fraction cutoff of 0.05. Differential expression thresholds were set to log fold-change >0.50 and p-value < 0.05 without adjustment, using top 250 targets per ligand. CellChat analysis was performed independently on ARIA− and ARIA+ subsets using the CellChatDB.human database. Communication probabilities were calculated for each ligand-receptor pair between cell types, filtering interactions with <10 cells per group. Pathway-level communication strengths were computed and network centrality scores were calculated. Merged CellChat objects enabled comparative analysis between conditions with network similarity computed for functional and structural properties. To investigate potential vascular-immune interactions, NicheNet v2.2.1 analysis was performed using endothelial cells from the reference dataset as sender cells and ARIA + CD8 + T cells as receivers. Differentially expressed genes from Fisher's meta-analysis of TEM and TEMRA CD8+ cells served as the gene set of interest. The top 20 ligands by corrected area under precision-recall curve were selected, with ligand-target relationships inferred using weighted networks (200 targets per ligand). CellChat analysis was performed on the integrated endothelial-CD8+ dataset using identical parameters to identify communication patterns between vascular and immune cell types.

External dataset validation

Cell type classifications were validated against published reference data[9] containing T cells from lecanemab-treated samples. Cross-dataset mapping was performed using k-nearest neighbor classification implemented in SCP v0.5.6. Correlation analysis used cosine similarity metrics with results displayed as annotated heatmaps. Validation focused on CD8 + T cell subset classifications to assess cross-study reproducibility. For vascular analysis, endothelial cells and inflammatory endothelial cells were subset from prefrontal cortex samples and integrated with ARIA + CD8 + T cells. The merged object was processed via principal component analysis and SCTransform normalization to correct for sequencing depth effects.

Data visualization and presentation

Single-cell data visualizations were generated using multiple complementary approaches. Dimensional reduction plots, expression distributions, and cell type comparisons were created using dittoSeq v1.18.0, SCP v0.5.6, and Seurat v5.3.0. Custom plots and statistical visualizations were generated using ggplot2 v3.5.2. Functional heatmaps for differential gene expression analysis were created using ComplexHeatmap v2.22.0 with expression data centered by gene across conditions (subtracting the mean expression for each gene) to highlight relative differences between ARIA+ and ARIA− samples.

Software and packages

Data analysis was performed using R version 4.4.2. Key software packages included: Seurat v5.3.0, scDblFinder v1.20.2, decontX v1.4.1, scCustomize v.3.2.4, scRepertoire v2.3.4, clusterProfiler v4.14.6, org.Hs.eg.db v3.20.0, AUCell v1.28.0, SCP v0.5.6, MultiNicheNet v2.1.0, CellChat v2.2.0, NicheNet v2.2.1, decoupleR v2.12.0, OmnipathR v3.15.99, dittoSeq v1.18.0, ggplot2 v3.5.2, ComplexHeatmap v2.22.0, Slingshot v2.14.0, NMF v0.28.

Statistical analysis

Statistical comparisons used Student's t-Test for pairwise contrasts, Wilcoxon rank-sum tests for continuous variables and chi-square tests for categorical data. Clonal expansion differences were assessed using bootstrap resampling (n = 10 iterations). Multiple testing correction used the Benjamini-Hochberg method where appropriate. All analyses were performed using the specified software packages. Statistical significance was defined as $p < 0.05$.

Sample size was determined by availability of matched case-control pairs meeting inclusion criteria (radiographically confirmed ARIA status, matched by sex, *APOE* genotype, age ± 5 years, and infusion number ± 1). No statistical method was used to predetermine sample size; this pilot study was designed as hypothesis-generating. No data were excluded from the analyses. The experiments were not randomized as this was an observational case-control study with prospective matching. Investigators were not blinded to group allocation during sample processing as ARIA status was known from clinical MRI; computational analyses were performed using anonymized sample identifiers.

The study included 6 participants (4 female, 2 male) aged 65–79 years. Sex was determined from clinical medical records. Both sexes were included in all analyses; the matched case-control design ensured sex balance between groups (2 female, 1 male per group). Given the small sample size (n = 3 per group), sex-stratified statistical analyses were not performed; future larger studies should examine potential sex-specific effects on ARIA-associated immune signatures. Disaggregated data are provided in the Source Data file.

All statistical tests were two-tailed unless otherwise specified. For patient-level comparisons (n = 3 vs n = 3), two-tailed Student's t-test was used. For single-cell differential expression analyses, Wilcoxon rank-sum tests were used with Benjamini-Hochberg correction for multiple comparisons; significance was defined as adjusted $p < 0.05$. Gene set enrichment analysis used two-tailed permutation tests (1000 permutations) with Benjamini-Hochberg correction. Pathway enrichment used hypergeometric tests (one-tailed, testing for over-representation) with Benjamini-Hochberg correction. All analyses were performed using R version 4.4.2 with packages described in the Methods.

Reporting summary

Further information on research design is available in the Nature Portfolio Reporting Summary linked to this article.

Data availability

The single-cell RNA sequencing, CITE-seq, and V(D)J data generated in this study have been deposited in the Gene Expression Omnibus (GEO) database under accession code GSE316096. Processed count matrices are publicly available; raw sequencing data are not available due to patient privacy considerations. Interactive data browsers for this study can be accessed at https://www.morgantilab.com/datasets. The metabolomics data generated in this study have been deposited in Metabolomics Workbench under accession code ST004524. The brain single-nucleus RNA sequencing data from lecanemab-treated patients used for cross-modal integration in this study are available in the GEO database under accession code GSE263079. Source data are provided with this paper.

Code availability

Customized analysis scripts used in this study are available from the corresponding author upon reasonable request.

References

1. van Dyck, C. H. et al. Lecanemab in Early Alzheimer's Disease. *N Engl J Med* **388**, 9–21 (2023).
2. Honig, L. S. et al. Updated safety results from phase 3 lecanemab study in early Alzheimer's disease. *Alzheimers Res Ther* **16**, 105 (2024).
3. Cummings, J. et al. Lecanemab: Appropriate Use Recommendations. *J Prev Alzheimers Dis* **10**, 362–377 (2023).
4. Kane, M. in *Medical Genetics Summaries* (eds V. M. Pratt et al.) (2012).
5. Cogswell, P. M. et al. Alzheimer Disease Anti-Amyloid Immunotherapies: Imaging Recommendations and Practice Considerations for Monitoring of Amyloid-Related Imaging Abnormalities. *American Journal of Neuroradiology* **46**, 24–32 (2025).
6. Reish, N. J. et al. Multiple Cerebral Hemorrhages in a Patient Receiving Lecanemab and Treated with t-PA for Stroke. *N Engl J Med* **388**, 478–479 (2023).
7. Solopova, E. et al. Fatal iatrogenic cerebral beta-amyloid-related arteritis in a woman treated with lecanemab for Alzheimer's disease. *Nat Commun* **14**, 8220 (2023).
8. Shields, L. B. E. et al. Initial Experience with Lecanemab and Lessons Learned in 71 Patients in a Regional Medical Center. *J Prev Alzheimers Dis* **11**, 1549–1562 (2024).
9. van Olst, L. et al. Microglial mechanisms drive amyloid-β clearance in immunized patients with Alzheimer's disease. *Nature Medicine* **31**, 1604–1616 (2025).
10. Sallusto, F., Lenig, D., Forster, R., Lipp, M. & Lanzavecchia, A. Two subsets of memory T lymphocytes with distinct homing potentials and effector functions. *Nature* **401**, 708–712 (1999).
11. Wherry, E. J. & Kurachi, M. Molecular and cellular insights into T cell exhaustion. *Nat Rev Immunol* **15**, 486–499 (2015).
12. Mills, E. L. et al. Itaconate is an anti-inflammatory metabolite that activates Nrf2 via alkylation of KEAP1. *Nature* **556**, 113–117 (2018).
13. Chang, C. H. et al. Posttranscriptional control of T cell effector function by aerobic glycolysis. *Cell* **153**, 1239–1251 (2013).
14. Cao, J. et al. Effects of altered glycolysis levels on CD8(+) T cell activation and function. *Cell Death Dis* **14**, 407 (2023).
15. McGettrick, A. F. & O'Neill, L. A. J. The Role of HIF in Immunity and Inflammation. *Cell Metab* **32**, 524–536 (2020).
16. Trapani, J. A. & Smyth, M. J. Functional significance of the perforin/granzyme cell death pathway. *Nat Rev Immunol* **2**, 735–747 (2002).
17. Intlekofer, A. M. et al. Effector and memory CD8+ T cell fate coupled by T-bet and eomesodermin. *Nat Immunol* **6**, 1236–1244 (2005).
18. Ingley, E. Functions of the Lyn tyrosine kinase in health and disease. *Cell Commun Signal* **10**, 21 (2012).
19. Menten, P., Wuyts, A. & Van Damme, J. Macrophage inflammatory protein-1. *Cytokine Growth Factor Rev* **13**, 455–481 (2002).
20. Gate, D. et al. Clonally expanded CD8 T cells patrol the cerebrospinal fluid in Alzheimer's disease. *Nature* **577**, 399–404 (2020).
21. Kasmani, M. Y. et al. Clonal lineage tracing reveals mechanisms skewing CD8+ T cell fate decisions in chronic infection. *J Exp Med* **220** https://doi.org/10.1084/jem.20220679 (2023).
22. Machado-Santos, J. et al. The compartmentalized inflammatory response in the multiple sclerosis brain is composed of tissue-resident CD8+ T lymphocytes and B cells. *Brain* **141**, 2066–2082 (2018).
23. Pereira, B. I. et al. Senescent cells evade immune clearance via HLA-E-mediated NK and CD8(+) T cell inhibition. *Nat Commun* **10**, 2387 (2019).
24. Jordao, M. J. C. et al. Single-cell profiling identifies myeloid cell subsets with distinct fates during neuroinflammation. *Science* **363** https://doi.org/10.1126/science.aat7554 (2019).
25. Goddery, E. N. et al. Microglia and Perivascular Macrophages Act as Antigen Presenting Cells to Promote CD8 T Cell Infiltration of the Brain. *Front Immunol* **12**, 726421 (2021).
26. Romagnoli, P. A., Premenko-Lanier, M. F., Loria, G. D. & Altman, J. D. CD8 T cell memory recall is enhanced by novel direct interactions with CD4 T cells enabled by MHC class II transferred from APCs. *PLoS One* **8**, e56999 (2013).
27. Ley, K., Laudanna, C., Cybulsky, M. I. & Nourshargh, S. Getting to the site of inflammation: the leukocyte adhesion cascade updated. *Nat Rev Immunol* **7**, 678–689 (2007).
28. Groom, J. R. & Luster, A. D. CXCR3 in T cell function. *Exp Cell Res* **317**, 620–631 (2011).
29. Jorfi, M. et al. Infiltrating CD8(+) T cells exacerbate Alzheimer's disease pathology in a 3D human neuroimmune axis model. *Nat Neurosci* **26**, 1489–1504 (2023).
30. van Olst, L. et al. Adaptive immune changes associate with clinical progression of Alzheimer's disease. *Mol Neurodegener* **19**, 38 (2024).
31. Chen, X. et al. Microglia-mediated T cell infiltration drives neurodegeneration in tauopathy. *Nature* **615**, 668–677 (2023).
32. Akbar, A. N. & Henson, S. M. Are senescence and exhaustion intertwined or unrelated processes that compromise immunity?. *Nat Rev Immunol* **11**, 289–295 (2011).
33. Henson, S. M., Riddell, N. E. & Akbar, A. N. Properties of end-stage human T cells defined by CD45RA re-expression. *Curr Opin Immunol* **24**, 476–481 (2012).
34. Pulko, V. et al. Human memory T cells with a naive phenotype accumulate with aging and respond to persistent viruses. *Nat Immunol* **17**, 966–975 (2016).
35. Ranasinghe, S. et al. Antiviral CD8(+) T Cells Restricted by Human Leukocyte Antigen Class II Exist during Natural HIV Infection and Exhibit Clonal Expansion. *Immunity* **45**, 917–930 (2016).
36. Wang, Z. et al. Clonally diverse CD38(+)HLA-DR(+)CD8(+) T cells persist during fatal H7N9 disease. *Nat Commun* **9**, 824 (2018).
37. Zhou, X. et al. MHC class II regulation of CD8(+) T cell tolerance and implications in autoimmunity and cancer immunotherapy. *Cell Rep* **42**, 113452 (2023).
38. Ramakrishnan, A. et al. Epigenetic dysregulation in Alzheimer's disease peripheral immunity. *Neuron* **112**, 1235–1248 e1235 (2024).
39. van Nierop, G. P. et al. Phenotypic and functional characterization of T cells in white matter lesions of multiple sclerosis patients. *Acta Neuropathol* **134**, 383–401 (2017).
40. Smolders, J. et al. Tissue-resident memory T cells populate the human brain. *Nat Commun* **9**, 4593 (2018).
41. Taylor, X. et al. Amyloid-beta (Abeta) immunotherapy induced microhemorrhages are linked to vascular inflammation and

cerebrovascular damage in a mouse model of Alzheimer's disease. *Mol Neurodegener* **19**, 77 (2024).
42. Gross, C. C. et al. CD8(+) T cell-mediated endotheliopathy is a targetable mechanism of neuro-inflammation in Susac syndrome. *Nat Commun* **10**, 5779 (2019).
43. Doedens, A. L. et al. Hypoxia-inducible factors enhance the effector responses of CD8(+) T cells to persistent antigen. *Nat Immunol* **14**, 1173–1182 (2013).
44. Pearce, E. L. Metabolism as a driver of immunity. *Nat Rev Immunol* **21**, 618–619 (2021).
45. Pearce, E. L. & Pearce, E. J. Metabolic pathways in immune cell activation and quiescence. *Immunity* **38**, 633–643 (2013).
46. Winford, E. et al. Terminally differentiated effector memory T cells associate with cognitive and AD-related biomarkers in an aging-based community cohort. *Immun Ageing* **21**, 36 (2024).
47. O'Sullivan, D. & Pearce, E. L. Targeting T cell metabolism for therapy. *Trends Immunol* **36**, 71–80 (2015).
48. Scharping, N. E. et al. The Tumor Microenvironment Represses T Cell Mitochondrial Biogenesis to Drive Intratumoral T Cell Metabolic Insufficiency and Dysfunction. *Immunity* **45**, 374–388 (2016).
49. Springer, T. A. Traffic signals for lymphocyte recirculation and leukocyte emigration: the multistep paradigm. *Cell* **76**, 301–314 (1994).
50. Groom, J. R. & Luster, A. D. CXCR3 ligands: redundant, collaborative and antagonistic functions. *Immunol Cell Biol* **89**, 207–215 (2011).

Acknowledgements

We are deeply grateful to the patients and their caregivers who generously participated in this study. Their willingness to contribute time and effort, often under challenging circumstances, made this work possible. We thank them for their trust and commitment to advancing our understanding of Alzheimer's disease and treatment-related complications. This work was supported by the National Institutes of Health, National Institute on Aging (R01AG081421 (LAJ), R01AG080589 (LAJ)), National Institute of Neurological Disorders and Stroke (RF1NS118558 (JMM)), National Center for Advancing Translational Sciences (TL1TR001997 (AVP)), the CNS Metabolism COBRE P20GM148326 (JMM, LAJ), and the Alzheimer's Association ABA-25-1376140 (LAJ, JMM).

Author contributions

L.A.J.: Conceptualization; Methodology; Investigation; Supervision; Writing-original draft; Writing-review & editing; Funding acquisition. K.S.: Formal analysis; Software; Visualization; Data curation; Writing-review & editing. A.V.P.: Investigation; Data curation; Writing-review & editing. J.L.F.: Investigation; Data curation; Writing-review & editing. A.R.E.: Resources; Investigation; Project administration; Writing-review & editing. C.L.S.: Resources; Investigation; Project administration; Writing-review & editing. D.A.H.: Methodology; Investigation; Data curation; Writing-review & editing. N.J.N.: Investigation; Data curation; Writing-review & editing. L.C.M.: Investigation; Data curation; Writing-review & editing. L.J.V.E.: Resources; Writing-review & editing. D.W.F.: Methodology; Writing-review & editing. G.E.C.: Conceptualization; Resources; Project administration; Writing-review & editing. J.M.M.: Conceptualization; Methodology; Investigation; Data curation; Formal analysis; Visualization; Writing-original draft; Writing-review & editing; Supervision; Funding acquisition.

Competing interests

The Authors have no competing interests to disclose.

Additional information

Supplementary information The online version contains supplementary material available at https://doi.org/10.1038/s41467-026-68921-3.

Correspondence and requests for materials should be addressed to Josh M. Morganti.

Peer review information *Nature Communications* thanks the anonymous reviewer(s) for their contribution to the peer review of this work. A peer review file is available.